Single-Shot Ultraviolet Compressed Ultrafast Photography

*Yingming Lai, Yujia Xue, Christian-Yves Côté, Xianglei Liu, Antoine Laramée, Nicolas Jaouen, François Légaré, Lei Tian, and Jinyang Liang**

Compressed ultrafast photography (CUP) is an emerging potent technique that allows imaging a nonrepeatable or difficult-to-produce transient event in a single shot. Despite many recent advances, existing CUP techniques operate only at visible and near-infrared wavelengths. In addition, spatial encoding via a digital micromirror device (DMD) in CUP systems often limits its field of view and imaging speeds. Finally, conventional reconstruction algorithms have limited control of the reconstruction process to further improve the image quality in the recovered (*x*, *y*, *t*) datacubes of the scene. To overcome these limitations, this article reports a single-shot UV-CUP that exhibits a sequence depth of up to 1500 frames with a size of 1750 × 500 (*x*, *y*) pixels at an imaging speed of 0.5 trillion frames per second. A patterned photocathode is integrated into a streak camera, which overcomes the previous restrictions in DMD-based spatial encoding and improves the system's compactness. Meanwhile, the plug-and-play alternating direction method of multipliers algorithm is implemented to CUP's image reconstruction to enhance reconstructed image quality. UV-CUP's single-shot ultrafast imaging ability is demonstrated by recording UV pulses transmitting through various spatial patterns. UV-CUP is expected to find many applications in both fundamental and applied science.

1. Introduction

Single-shot ultrafast optical imaging is of great significance in revealing the fundamental mechanisms in physics, chemistry, and biology.[1] Unlike the multiple-shot counterpart[2–4] that applies only to repeatable phenomena, single-shot ultrafast optical imaging can record transient events that are nonrepeatable or difficult to produce.[5–7] Depending on the image acquisition methods, existing single-shot ultrafast optical imaging techniques can be divided into the active-detection category and the passive-detection category.[1] The former[8–11] uses specially designed pulse trains to probe transient events, while the latter[12–14] exploits receive-only ultrafast detectors to record photons from dynamic scenes. Circumventing the active illumination, the passive-detection scheme is well suited in imaging self-luminescent and color-selective transient events.

Among existing passive-detection approaches, compressed ultrafast photography (CUP) has attracted tremendous research interests. By integrating compressed sensing into streak imaging, the CUP system allows recording a 3D spatiotemporal (*x*, *y*, *t*) datacube of a transient event in a single camera exposure.[12] Since CUP's invention in 2014, many technical innovations in optical instrumentation have been made to improve the system's performance. For example, a femtosecond streak camera assisted CUP in achieving an imaging speed of 70 trillion frames per second (Tfps).[15] Moreover, wide-field microscopy and phase-contrast imaging modalities were integrated into CUP to provide high spatial resolution and new contrast.[16] Furthermore, a galvanometer scanner replaced the streak camera to enable all-optical operation in CUP,[17] which extended the technique's applicability to most charge-coupled device (CCD) and CMOS (complementary metal oxide semiconductor) cameras. Finally, several configurations were proposed for CUP-based electron imaging.[18,19]

Advances in reconstruction algorithms have also enhanced CUP's performance. For example, space and intensity constraints[20] were added into the original reconstruction algorithm based on the two-step iterative shrinkage/thresholding (TwIST) algorithm[21] to mitigate the low-intensity artifacts. Moreover, an augmented Lagrangian algorithm was developed to decrease the dependence of the regularizer in the TwIST algorithm to the content in the dynamic scene.[22] Finally, a genetic algorithm[23] and a gradient descent algorithm[18] were implemented to increase the incoherence between the spatial encoding mask and the sparse basis of the scene.

Y. Lai, X. Liu, A. Laramée, Prof. F. Légaré, Prof. J. Liang
Centre Énergie Matériaux Télécommunications
Institut National de la Recherche Scientifique
1650 boulevard Lionel-Boulet, Varennes, Québec J3X1S2, Canada
E-mail: jinyang.liang@emt.inrs.ca

Y. Xue, Prof. L. Tian
Department of Electrical and Computer Engineering
Boston University
8 St. Mary's Street, Boston, MA 02215, USA

C.-Y. Côté
Axis Photonique Inc.
1650 boulevard Lionel-Boulet
Varennes Québec J3X1S2, Canada

Dr. N. Jaouen
Beamline SEXTANTS
Synchrotron SOLEIL
L'Orme des Merisiers
St-Aubin, BP 48, Gif-sur-Yvette 91192, France

The ORCID identification number(s) for the author(s) of this article can be found under https://doi.org/10.1002/lpor.202000122

DOI: 10.1002/lpor.202000122

These innovations in hardware and algorithms, in turn, have facilitated CUP in finding new applications. Among them, CUP is popularly implemented to real-time visualization of light dynamics, such as the faster-than-light traveling of noninformation,[12] the propagation of a photonic Mach cone in scattering medium,[24] and the temporal focusing of a femtosecond laser pulse.[25] Moreover, CUP has benefited many derivative technologies, including improving the acquisition rate in fluorescent lifetime imaging,[26] achieving wide-field time-of-flight volumetric imaging,[27] and assisting in secured quantum communication.[28]

Despite these remarkable accomplishments, current CUP technologies are limited in several aspects. First, CUP has been experimentally demonstrated only in the visible and near-infrared spectral ranges. The lack of imaging capability in the UV spectrum excludes CUP from imaging many scientifically important transient phenomena, such as UV pulse generation via four-wave mixing[29] and the formation-relaxation dynamics of UV-pulse-induced absorbing defects in potassium dihydrogen phosphate crystals.[30] Second, most CUP systems use a digital micromirror device (DMD) to spatially encode the dynamic event. As a programmable binary-amplitude spatial light modulator,[31,32] the DMD consists of up to several millions of individually addressable micromirrors, each of which has a +12° or −12° tilt angle with respect to the device's surface normal. As a result, the DMD is often required to be placed in the Littrow configuration in CUP systems to retro-reflect the incident light.[12,15,17,20,22,23,27] This design, despite offering good encoding adaptability, restricts the field of view (FOV) and the imaging speed of CUP. Although these constraints can be overcome by replacing the DMD with a transmissive mask[23] or by using the loss-less encoding configuration,[16] these systems are still bulky, which could hinder CUP's applicability to various field studies that require restricted weight and size of the deployed instrument.[33] Finally, the conventional TwIST algorithm with a total variation (TV) regularizer is still the mainstream in CUP's image reconstruction. However, it is well known that the TV regularization tends to introduce staircasing artifacts in the reconstruction,[34] which limits the spatial and temporal resolutions as well as produces considerable anisotropy in spatial resolutions between the x and y dimensions (e.g., 19.4% in ref. [12]). Thus, the existing image reconstruction paradigm restricts the quality of the image reconstruction and the type of transient objects that can be reliably reconstructed.

2. Experimental Section

2.1. System Schematic and Data Acquisition

To overcome these limitations, we have developed single-shot UV-CUP. As shown in **Figure 1**a, a dynamic event, $I(x, y, t)$, is imaged by the front optics to the entrance port (41 mm in diameter) of a customized streak camera (AXIS-2DX, Axis Photonique), whose intrinsic spatial and temporal resolutions are 36 μm and 6 ps, respectively. The image is further relayed by the input optics to a patterned palladium photocathode (35 mm × 10 mm in size and 200–270 nm in sensing wavelength range) that is fabricated by lithography. As illustrated in Figure 1b, a 200 nm thick layer of chromium is deposited on a 1.5 mm thick fused silica substrate by electron-beam evaporation. A pseudo-random binary pattern (Figure 1c), with each encoding pixel having an 80 μm × 80 μm size, is engraved using a laser lithography process. In this way, the photons in the dynamic event are spatially encoded, which is denoted by the operator **C**. Then, a layer of palladium with a thickness of 8.5 nm is deposited by electron-beam evaporation on top of the chromium layer to convert photons into photoelectrons. Next, the photoelectrons gain velocity by a pulling voltage applied to an acceleration mesh. Subsequently, they pass through a time-varying electric field applied to a pair of sweep electrodes. According to the time-of-arrival, these photoelectrons are deflected to different spatial positions along the vertical axis (i.e., the y-axis in Figure 1a). This process is denoted by the temporal shearing operator **S**. Afterward, the photoelectrons in the spatially encoded and temporally sheared scene are converted back to photons by a phosphor screen, followed by a fiber taper that relays the image onto an internal CCD camera ($N_r \times N_c = 2000 \times 2000$ binned pixels (2 × 2 binning), the subscripts "r" and "c" denote "row" and "column," respectively). The CCD camera records the data by spatially integrating over each pixel and temporally integrating over the exposure time, which is denoted by the spatiotemporal integration operator **T**. The captured snapshot is denoted by $E(m, n)$, where m and n represent the indices of pixels in the x and y axes. Overall, UV-CUP's data acquisition process can be described by a forward model as

$$E(m, n) = \mathbf{TSC}I(x, y, t) \tag{1}$$

2.2. Image Reconstruction

In image reconstruction, $I(x, y, t)$ is recovered by solving a regularized least-squares optimization problem.[35] Here, we develop a novel CUP reconstruction algorithm based on the framework of the plug-and-play alternating direction method of multipliers (PnP-ADMM) algorithm[36,37]

$$\hat{I} = \arg\min_{I,v,u,w} \left\{ \frac{1}{2}\|E - \mathbf{T}v\|_2^2 + R(u) + \mathrm{I}_+(w) + \frac{\mu_1}{2}\left\|\mathbf{SC}I - v + \frac{\gamma_1}{\mu_1}\right\|_2^2 + \frac{\mu_2}{2}\left\|I - u + \frac{\gamma_2}{\mu_2}\right\|_2^2 + \frac{\mu_3}{2}\left\|I - w + \frac{\gamma_3}{\mu_3}\right\|_2^2 \right\} \tag{2}$$

Here $\|\cdot\|_2$ represents the l_2 norm. $R(\cdot)$ is the implicit regularizer. $\mathbf{I}_+(\cdot)$ represents a nonnegative indicator function. v, u, and w are primal variables. γ_1, γ_2, and γ_3 are dual variables. μ_1, μ_2, and μ_3 are penalty parameters.[38,39] The main advantages of PnP-ADMM CUP algorithm over existing CUP reconstruction paradigms are manifested in twofold. First, the variable splitting strategy is carefully designed to enable fast, closed-form solutions to the sub-optimization in the PnP-ADMM update routine. Second, the PnP-ADMM CUP algorithm allows us to use state-of-the-art denoising algorithms

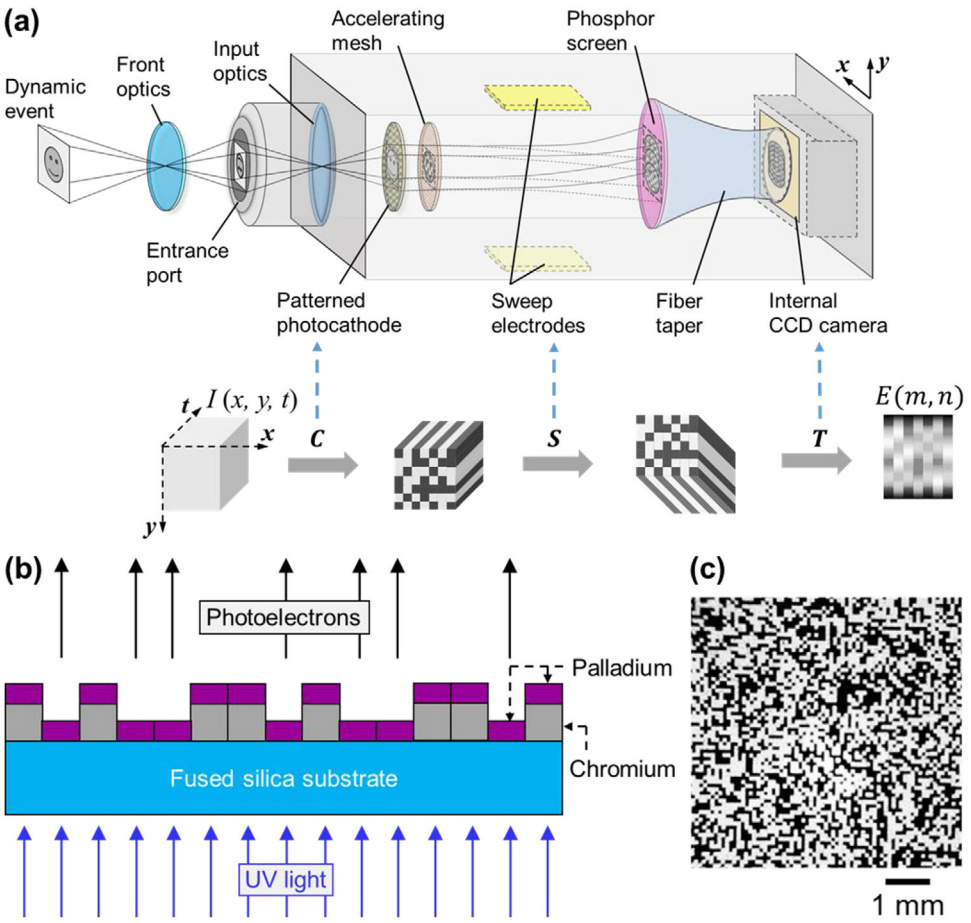

Figure 1. Operating principle of UV-CUP. a) System schematic and data acquisition. b) Cross-section of the patterned photocathode. c) Partial view of the encoding mask.

beyond the classical TV denoiser to achieve superior reconstruction results. Specifically, we implement the sub-optimization over $R(\cdot)$ with the block-matching and 3D filtering (BM3D) denoiser,[38] which has shown to provide superior performance for a wide class of natural objects for solving similar inverse problems.[40–42]

The initialization of the PnP-ADMM algorithm is conducted as follows. Let N_x, N_y, and N_t be the numbers of pixels in the reconstructed (x, y, t) datacube. The operator $\mathbf{C}$ is obtained by measuring the encoded mask, which has dimensions of $N_x \times N_y$. The shearing operator $\mathbf{S}$ is $N_x \times (N_y + N_t - 1) \times N_t$ in size. Its first frame is constructed by padding $(N_t - 1)$ rows of zeros below the matrix of the operator $\mathbf{C}$. The next frame is generated by circulantly shifting the first frame downward by one pixel. This process is repeated by $(N_t - 1)$ times until the matrix of the spatial encoding operator reaches the bottom of the frame. The integration operator $\mathbf{T}$ performs a summation along the t axis. I^0, ${\gamma_1}^0$, ${\gamma_2}^0$, and ${\gamma_3}^0$ are set to zero matrices with dimensions $N_x \times N_y \times N_t$. ${\mu_1}^0$, ${\mu_2}^0$, and ${\mu_3}^0$ are set to 1. These inputs, along with the acquired single image $E(m, n)$, are fed to the PnP-ADMM algorithm, which iteratively updates the primal variable as well as the estimated datacube via the following steps as the flowchart shown in **Figure 2**.

Step 1: update primal variables (i.e., v, u, and w) by

$$v^{k+1} = (\mathbf{T}^T \cdot \mathbf{T} + \mu_1^k U)^{-1} \cdot (\mathbf{T}^T E + \mu_1^k \mathbf{S}\mathbf{C} I^k + \gamma_1^k),$$
$$u^{k+1} = D_{BM3D}\left(I^k + \frac{\gamma_2^k}{\mu_2^k}\right), \text{and}$$
$$w^{k+1} = \max\left\{0, I^k + \frac{\gamma_3^k}{\mu_3^k}\right\} \quad (3)$$

Here, U is the identity matrix. $D_{\text{BM3D}}(\cdot)$ stands for the BM3D denoiser.

Step 2: update the estimated datacube of the dynamic event (i.e., I) by

$$I^{k+1} = (\mu_1^k \mathbf{S}^T \cdot \mathbf{C}^T \cdot \mathbf{C} \cdot \mathbf{S} \cdot U + \mu_2^k U + \mu_3^k U)^{-1} \cdot \left[\mu_1^k (\mathbf{S}\mathbf{C})^T \left(v^{k+1} - \frac{\gamma_1^k}{\mu_1^k}\right) + \mu_2^k \left(u^{k+1} - \frac{\gamma_2^k}{\mu_2^k}\right) + \mu_3^k \left(w^{k+1} - \frac{\gamma_3^k}{\mu_3^k}\right)\right] \quad (4)$$

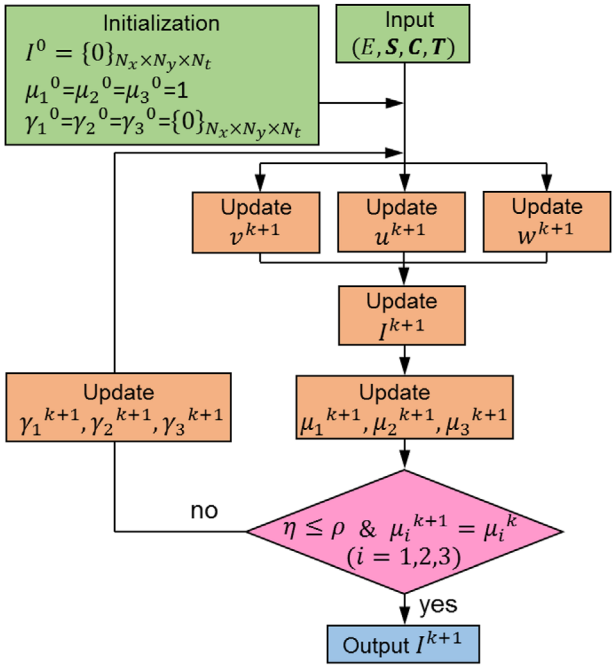

Figure 2. Flowchart of the PnP-ADMM algorithm for UV-CUP's image reconstruction.

Step 3: update the penalty parameters (i.e., μ_1, μ_2, and μ_3) by

$$\mu_i^{k+1} = \begin{cases} \tau\mu_i^k, & \text{if } p > \sigma q \\ \dfrac{\mu_i^k}{\tau}, & \text{if } \sigma p < q \\ \mu_i^k, & \text{otherwise} \end{cases} \quad (i = 1, 2, 3) \tag{5}$$

Here, $p = \|I^{k+1} - v^{k+1}\|_2$ is the primal residual and $q = \mu_i^k \|I^{k+1} - I^k\|_2$ is the dual residual. $\tau(\tau > 1)$ is the balancing factor, and $\sigma(\sigma > 1)$ is the residual tolerance.[43] In our experiments, we chose τ =1.1 and σ =1.5.

Step 4: judge the relative change in results and the parameters μ_1^{k+1}, μ_2^{k+1}, and μ_3^{k+1} in adjacent iterations by

$$\text{if } \eta = \frac{I^{k+1} - I^k}{I^k} < \rho \text{ and } \mu_i^{k+1} = \mu_i^k (i = 1, 2, 3) \tag{6}$$

Here, $\rho(0 < \rho < 10^{-3})$ is the pre-set tolerance value.

Step 5: if the convergence is unmet, update dual variables (i.e., γ_1, γ_2, and γ_3) by

$$\begin{aligned} \gamma_1{}^{k+1} &= \gamma_1{}^k + \mu_1^{k+1}\left(\mathbf{S}\mathbf{C}I^{k+1} - v^{k+1}\right), \\ \gamma_2{}^{k+1} &= \gamma_2{}^k + \mu_2^{k+1}(I^{k+1} - u^{k+1}), \text{and} \\ \gamma_3{}^{k+1} &= \gamma_3{}^k + \mu_3^{k+1}(I^{k+1} - w^{k+1}) \end{aligned} \tag{7}$$

These steps are repeated until all criteria in Step 4 are satisfied. The image reconstruction recovers the spatiotemporal datacube of the dynamic scene. The output movie has a sequence depth (i.e., the maximum number of frames in the movie) of $N_t = 1500$ frames, each of which has a size of $N_x \times N_y = 1750 \times 500$ pixels. The imaging speed of UV-CUP, R, is calculated by

$$R = s/d_b \tag{8}$$

where s = 9 mm ns^{-1} is the shearing speed, and d_b = 18 μm is the binned pixel size of the internal CCD camera. Thus, UV-CUP's imaging speed is R = 0.5 Tfps.

3. Results

3.1. Evaluation of PnP-ADMM-Based Image Reconstruction

To demonstrate the superior performance of the PnP-ADMM algorithm to the TwIST algorithm, we compared the reconstructed image qualities using a simulated dynamic event, namely, a static "Mandrill" image with the intensity changing as a Gaussian function. The event datacube had a sequence depth of 40 frames, each of which had 512 × 512 (x, y) pixels. The simulated snapshot, E_s, was obtained by applying the forward model (i.e., Equation (1)) to this event. E_s was input to both the PnP-ADMM algorithm and the TwIST algorithm for image reconstruction. The initialization of the PnP-ADMM algorithm was detailed in Section 2.2. For the TwIST algorithm, the weighting parameter for the regularizer was set to 0.2.

The reconstructed images (see the full evolution in Video S1, Supporting Information) from both algorithms are compared in **Figure 3**. In particular, Figure 3a shows the 21st frames of the ground truth, TwIST reconstruction, and PnP-ADMM reconstruction. Zoomed-in views of the three areas in the ground truth and in the reconstructed results are shown in Figure 3b. These results reveal that PnP-ADMM can accurately recover the spatial details, while the TwIST reconstructed images appear blurred with many spatial features lost. To quantitatively evaluate the performance, we analyzed 3 dB bandwidths of the Fourier spectra of the three images in Figure 3a. The results are shown in Figure 3c. The profiles of normalized power spectrum density in x and y axes from these results are compared in Figure 3d. The TwIST algorithm reduces the spatial bandwidth by 33.3% and 47.3% in the x and y axes, respectively. In contrast, PnP-ADMM degrades the bandwidths by 12.1% and 16.4%. Therefore, PnP-ADMM allows a more reliable reconstruction in UV-CUP. Moreover, the resolution anisotropy between the x and y dimensions of TwIST-based reconstruction is 21.0%, while the PnP-ADMM-based reconstruction produces 4.9%. Thus, PnP-ADMM shows superior performance in suppressing resolution anisotropy.

3.2. Quantification of Spatial and Temporal Resolutions

To characterize the spatial and temporal resolutions of the UV-CUP system, we imaged a dynamic scene of two 1 μJ UV laser pulses sequentially transmitting through a cross-wire target (**Figure 4**a). In the experimental setup, an 800 nm femtosecond laser pulse was converted to a 266 nm UV pulse with the same pulse width via second harmonic generation and subsequent sum-frequency generation. The UV pulse was then equally split into two arms by a beam splitter. In each arm, the laser pulse was retro-reflected by a mirror. A manual translation stage was added

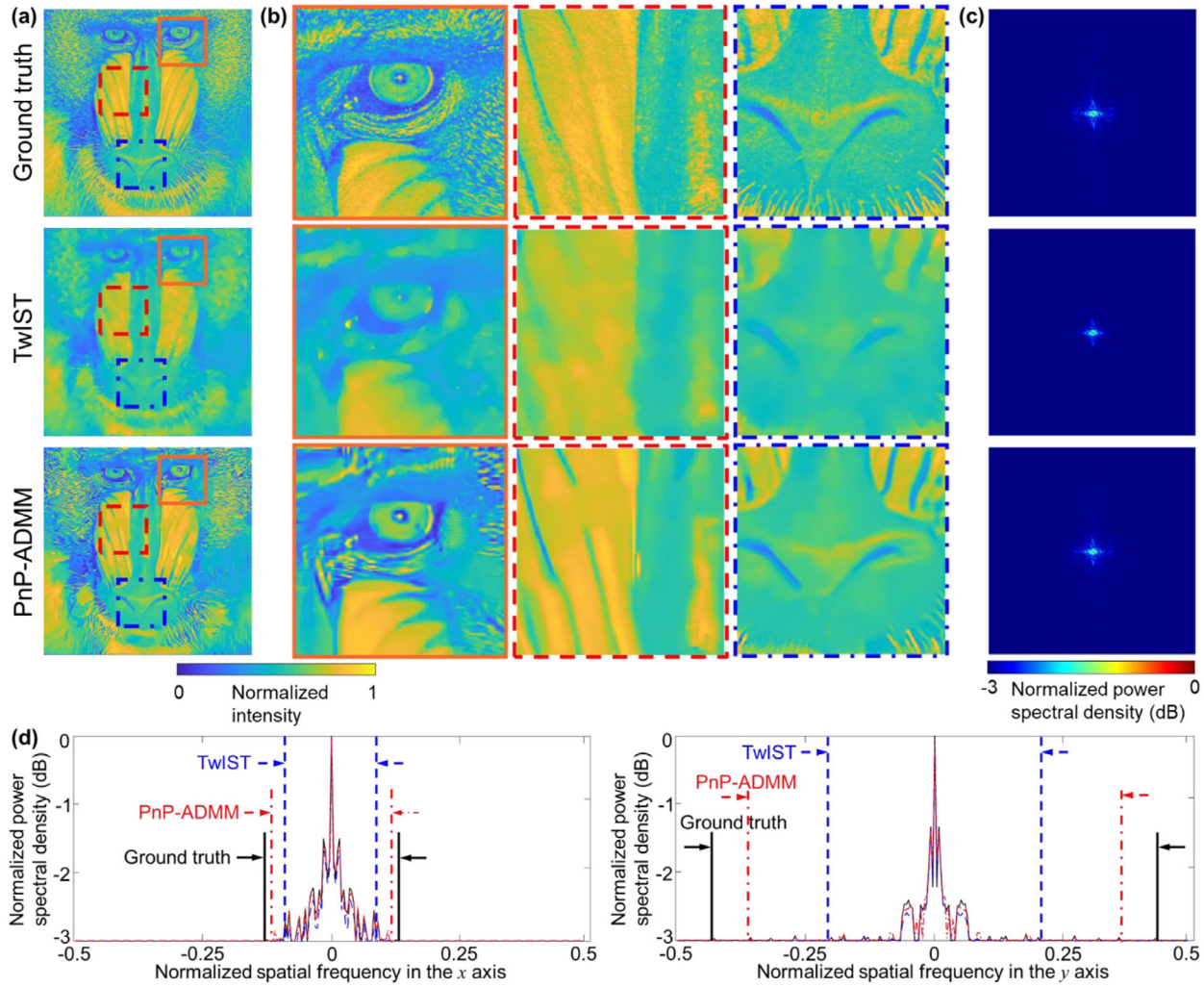

Figure 3. Comparison of the ground truth with the reconstructions using the TwIST algorithm and the PnP-ADMM algorithm. a) The 21st frame in the dynamic scene. b) Zoomed-in views of three selected areas (marked in the first panel in (a)). c) Spatial frequency distributions of the images in (a). d) Cross-sections of the normalized power spectral density in the *x* and *y* axes of the images in (c).

into one arm to generate a tunable optical delay of up to 100 ps. For spatial resolution quantification, the two daughter pulses with a 35 ps time delay propagated collinearly to a spatial pattern composed of two crossed 600 μm diameter wires. The UV-CUP system, synchronized with the laser, captured this event in a single shot. Figure 4b presents the reconstructed results in six selected frames, showing the temporal intensity changes of laser pulses whose shapes were modulated by the crossed wires (see the full evolution in Video S2, Supporting Information). Selected cross-sections along the horizontal and vertical directions in the frame at $t = 54$ ps were extracted, as shown in Figure 4c. To quantify the spatial resolution, the calibration of the nonuniform intensity distribution of the laser pulse was applied to the reconstructed image. Then, the line profiles of the wire's edge were averaged to calculate the edge spread function (ESF). Taking the derivative of the ESF yielded the line spread function (LSF). The spatial resolutions of the UV-CUP system, defined by the full-widths at half-maximum (FWHMs) of the fitted LSFs in the horizontal and vertical directions, were determined to be 99 and 109 μm, respectively (Figure 4d). The resolution anisotropy was determined to be 10.1%. This result echoes PnP-ADMM's superior performance in suppressing the resolution anisotropy as demonstrated in Section 3.1. To obtain the temporal resolution, we imaged the same event with seven time-delays Δt ranged from 5 to 60 ps (Figure 4e). Three measurements were acquired for each time delay. We did not observe any unwanted surface reflections from optical components. Representative time courses of normalized average intensity with different time delays are plotted as the inset of Figure 4e. ΔI is defined as the intensity dip at the half of Δt. The experimental result was fitted with a model that represents incoherent addition of two identical Gaussian functions with normalized intensities with the time delay of Δt, i.e.,

$$\Delta I(\Delta t) = \begin{cases} 1 - 2\exp\left[-\ln(2)\frac{\Delta t^2}{a^2}\right], & (\Delta I > 0) \\ 0, & \text{otherwise} \end{cases} \tag{9}$$

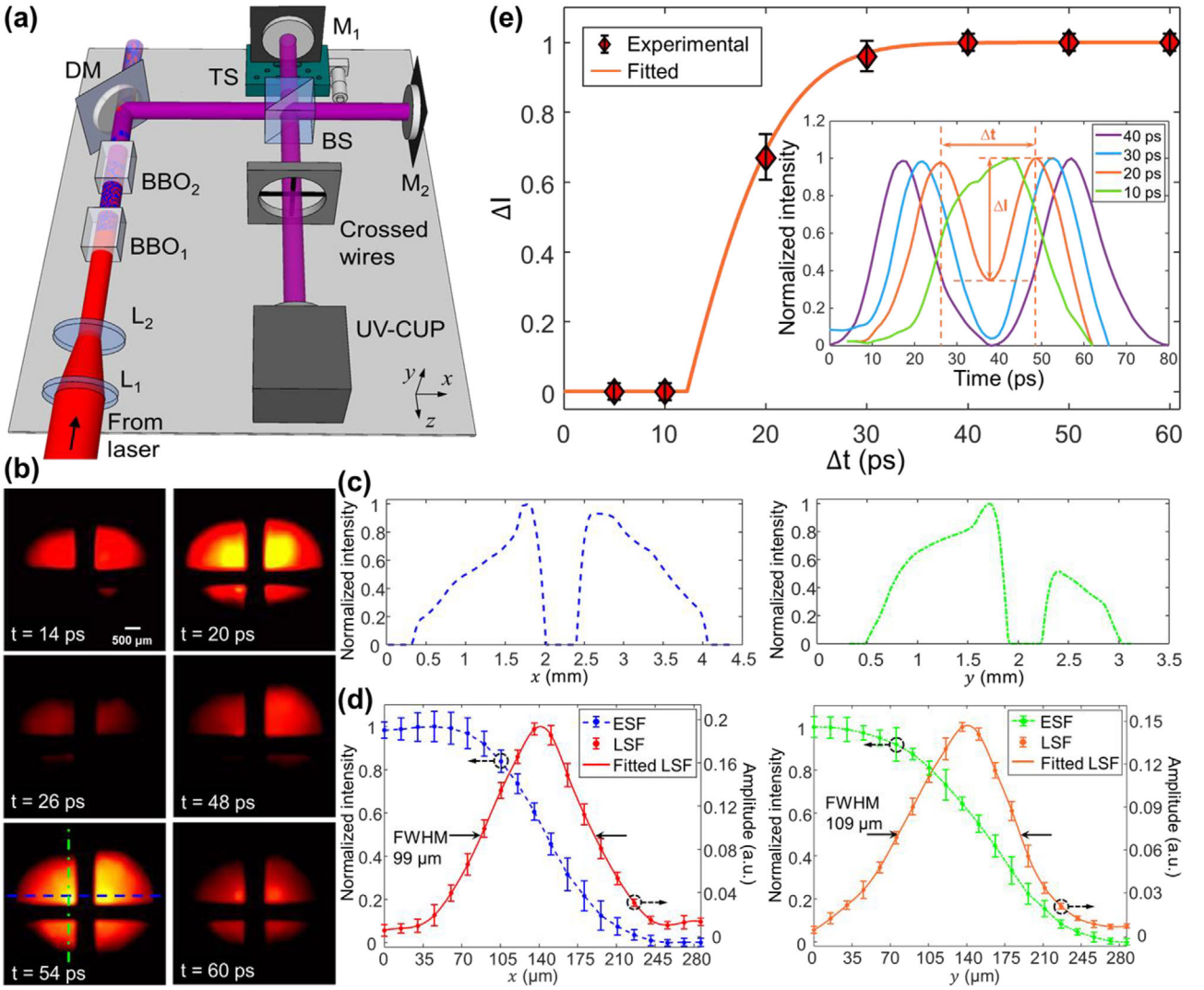

Figure 4. Characterization of spatial and temporal resolutions of the UV-CUP system. a) Experimental setup. BBO_1-BBO_2, barium borate crystal; BS, beam splitter; DM, dichroic mirror; L_1–L_2, lens; M_1–M_2, mirror; TS, translation stage. b) Six representative frames of the reconstruction scenes, where two spatially modulated UV pulses had a 35 ps time delay. c) Intensity profiles of two cross-sections marked in (b). d) Analysis of the spatial resolution in the horizontal and vertical directions. The LSFs were fitted by cubic spline interpolation. Error bar: standard deviation. e) Analysis of the temporal resolution. Error bar: standard deviation. Inset: Time courses of averaged laser intensity of the two pulses with different pulse delays.

where a is the FWHM of the reconstructed time course. The temporal resolution of the UV-CUP system, defined by Δt that gives $\Delta I \leq 0.25$, was quantified to be 14 ps.

3.3. Visualization of Transmissive Targets

To demonstrate UV-CUP's 2D imaging capability, we imaged two spatially and temporally separated UV pulses transmitting through hollow patterns that contain engraved letters of "INRS" and "AXIS". The two UV pulses had a 40 ps time delay. The mirror M_2 was slightly tilted with respect to the normal of the incident beam to generate a lateral shift to the reflected pulse (**Figure 5**a). The reconstructed movies are shown in Videos S3 and S4 in the Supporting Information. Figure 5b–e presents the reconstructed results of "INRS" and "AXIS" at two specific time points. Representative cross-sections show good conformity with the pulses' intensity profiles.

4. Conclusions and Discussion

We have demonstrated CUP in the UV spectral range for the first time. The UV-CUP system was constructed by integrating a patterned photocathode into a streak camera. Therefore, this compact design is not subject to the limitations in FOV and imaging speeds imposed by the tilted DMD in previous CUP systems. Moreover, the PnP-ADMM algorithm was implemented, for the first time, to improve the quality of CUP's image reconstruction. At an imaging speed of 0.5 Tfps, the UV-CUP system can record up to 1500 frames, each of which has 1750 × 500 (x, y) pixels in size. The system's spatial and temporal resolutions, determined

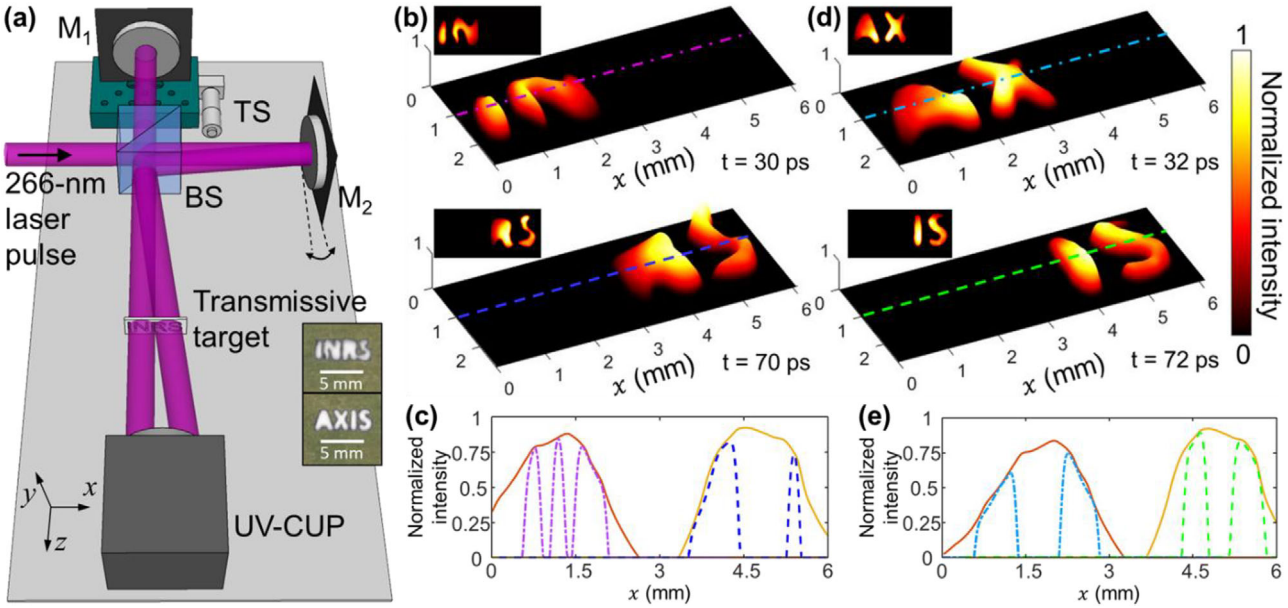

Figure 5. Single-shot UV-CUP of two UV pulses transmitting through spatial targets. a) Experimental setup. b) Representative (x, y) frames of laser pulses transmitting through the target containing letters "INRS". c) Cross-sections marked in (b) with comparing to incident pulses' intensity profiles. d) As (b), but with the target "AXIS". e) As (c), but shows the results marked in (d). The orange and the yellow solid lines in (c) and (e) represent the intensity profiles of the first and the second pulses.

by the overall magnification ratio and the sweep voltage, were quantified to 99 μm in the x-axis, 109 μm in the y-axis, and 14 ps, respectively. UV-CUP's single-shot ultrafast imaging ability was demonstrated by capturing the transmission of UV pulses through spatial patterns.

In the UV-CUP system, the size of encoding pixels on the palladium photocathode was determined jointly by the noise performance and the design of the streak camera. Due to the limited quantum yield of the palladium photocathode to the 266 nm light, the signal-to-noise ratio (SNR) in the acquired raw data was moderate. Thus, 2×2 pixel binning was used in the internal CCD camera to improve the image quality. Moreover, considering the 0.92 × magnification ratio of the streak camera and the Nyquist sampling theory, each encoding pixel should have a size of at least ~40 μm × 40 μm. Finally, the design needs to facilitate the reconstruction algorithm to accurately identify the encoding mask under the limited SNR. Therefore, we chose the size of the 80 μm × 80 μm for the encoding pixels, which balances the image reconstruction reliability with the spatial and temporal resolutions.

The PnP-ADMM-based image reconstruction shows its superior performance, adaptability, and potential. By splitting the overall optimization into several secondary minimization problems (i.e., Equation (2)) and precisely solving them in parallel with the flexibility to incorporate state-of-the-art denoising algorithm, PnP-ADMM improves the quality of reconstructed image than conventional TwIST algorithm. PnP-ADMM assisted UV-CUP in increasing the spatiotemporal resolutions, suppressing the resolution anisotropy, and reconstructing spatial features without artifacts. Despite only demonstrated in the UV-CUP system, the PnP-ADMM-based image reconstruction is universally adaptable to other CUP systems for diverse experiments. Especially for high SNRs in the acquired data, the reconstructed image quality is critically determined by the software. The PnP-ADMM-based image reconstruction can outperform the TwIST algorithm in recovering dynamic scenes with complex spatiotemporal features.

Future investigations will be carried out in both technical improvement and application exploration. For example, by adopting streak cameras with optical shearing units[17] and by using photocathodes with higher quantum efficiencies at the targeted UV wavelengths,[44] SNRs in the acquired raw data can be improved, which can allow using a smaller encoding pixel and thus preserving more spatiotemporal features in the image reconstruction. In this way, UV-CUP's spatial and temporal resolutions could be further boosted. In addition, other photosensitive materials (e.g., gallium nitride[45] whose sensing spectrum is 150–400 nm) could be used in the fabrication of the patterned photocathode sensing other UV wavelengths. In software, the quality of the reconstruction may be further improved by incorporating state-of-the-art deep-learning-based denoisers into the PnP-ADMM framework.[46,47] UV-CUP will open up many new possibilities in single-shot observation of transient UV phenomena, including laser-induced UV plasma emission[48] and UV-fluorescence in graphene oxides.[49]

Supporting Information

Supporting Information is available from the Wiley Online Library or from the author.

Acknowledgements

This work was supported by Natural Sciences and Engineering Research Council (NSERC) of Canada (RGPIN-2017-05959, RGPAS-507845-2017,

CRDPJ-532304-18, RTI-2018-00505); Canada Foundation for Innovation (37146); Fonds de Recherche du Québec - Nature et Technologies (FRQNT; 2019-NC-252960); Fonds de Recherche du Québec - Santé (FRQS; 280229, 267406); and National Science Foundation (1813848).

Conflict of Interest

The authors declare no conflict of interest.

Keywords

compressed ultrafast photography, image reconstruction techniques, plug-and-play alternating direction method of multipliers algorithm, single-shot ultrafast imaging, ultraviolet

Received: March 27, 2020
Revised: July 21, 2020
Published online: September 13, 2020

[1] J. Y. Liang, L. V. Wang, *Optica* **2018**, *5*, 1113.
[2] M. L. M. Balistreri, H. Gersen, J. P. Korterik, L. Kuipers, N. F. van Hulst, *Science* **2001**, *294*, 1080.
[3] G. Gariepy, N. Krstajic, R. Henderson, C. Y. Li, R. R. Thomson, G. S. Buller, B. Heshmat, R. Raskar, J. Leach, D. Faccio, *Nat. Commun.* **2015**, *6*, 6362.
[4] L. Fieramonti, A. Bassi, E. A. Foglia, A. Pistocchi, C. D'Andrea, G. Valentini, R. Cubeddu, S. De Silvestri, G. Cerullo, F. Cotelli, *PLoS One* **2012**, *7*, e50744.
[5] D. R. Solli, C. Ropers, P. Koonath, B. Jalali, *Nature* **2007**, *450*, 1054.
[6] S. S. Howard, A. Straub, N. Horton, D. Kobat, C. Xu, *Nat. Photonics* **2013**, *7*, 33.
[7] M. Dong, S. Husale, O. Sahin, *Nat. Nanotechnol.* **2009**, *4*, 514.
[8] X. F. Wang, L. H. Yan, J. H. Si, S. Matsuo, H. L. Xu, X. Hou, *Appl. Opt.* **2014**, *53*, 8395.
[9] Z. Li, R. Zgadzaj, X. Wang, Y. Y. Chang, M. C. Downer, *Nat. Commun.* **2014**, *5*, 3085.
[10] K. Nakagawa, A. Iwasaki, Y. Oishi, R. Horisaki, A. Tsukamoto, A. Nakamura, K. Hirosawa, H. Liao, T. Ushida, K. Goda, F. Kannari, I. Sakuma, *Nat. Photonics* **2014**, *8*, 695.
[11] Y. Lu, T. T. W. Wong, F. Chen, L. V. Wang, *Phys. Rev. Lett.* **2019**, *122*, 193904.
[12] L. Gao, J. Y. Liang, C. Y. Li, L. V. Wang, *Nature* **2014**, *516*, 74.
[13] T. G. Etoh, D. V. Son, T. Yamada, E. Charbon, *Sensors* **2013**, *13*, 4640.
[14] V. Tiwari, M. A. Sutton, S. R. McNeill, *Exp. Mech.* **2007**, *47*, 561.
[15] P. Wang, J. Y. Liang, L. V. Wang, *Nat. Commun.* **2020**, *11*, 2091.
[16] T. Kim, J. Y. Liang, L. Zhu, L. V. Wang, *Sci. Adv.* **2020**, *6*, eaay6200.
[17] X. Liu, J. Liu, C. Jiang, F. Vetrone, J. Y. Liang, *Opt. Lett.* **2019**, *44*, 1387.
[18] X. Liu, S. Zhang, A. Yurtsever, J. Y. Liang, *Micron* **2019**, *117*, 47.
[19] D. L. Qi, C. S. Yang, F. Y. Cao, J. Y. Liang, Y. L. He, Y. Yang, T. Q. Jia, Z. R. Sun, S. A. Zhang, *Phys. Rev. Appl.* **2018**, *10*, 054061.
[20] L. Zhu, Y. Chen, J. Y. Liang, Q. Xu, L. Gao, C. Ma, L. V. Wang, *Optica* **2016**, *3*, 694.
[21] J. M. Bioucas-Dias, M. A. Figueiredo, *IEEE Trans. Image Process.* **2007**, *16*, 2992.
[22] C. S. Yang, D. L. Qi, F. Y. Cao, Y. L. He, X. Wang, W. L. Wen, J. S. Tian, T. Q. Jia, Z. R. Sun, S. A. Zhang, *J. Opt.* **2019**, *21*, 035703.
[23] C. S. Yang, D. L. Qi, X. Wang, F. Y. Cao, Y. L. He, W. L. Wen, T. Q. Jia, J. S. Tian, Z. R. Sun, L. Gao, S. A. Zhang, L. V. Wang, *Optica* **2018**, *5*, 147.
[24] J. Y. Liang, C. Ma, L. Zhu, Y. Chen, L. Gao, L. V. Wang, *Sci. Adv.* **2017**, *3*, e1601814.
[25] J. Y. Liang, L. Zhu, L. V. Wang, *Light: Sci. Appl.* **2018**, *7*, 42.
[26] J. Thompson, J. Mason, H. Beier, J. Bixler, *Proc. SPIE* **2017**, *10076*, 1007613.
[27] J. Y. Liang, L. Gao, P. F. Hai, C. Y. Li, L. V. Wang, *Sci. Rep.* **2015**, *5*, 15504.
[28] C. Yang, Y. Ding, J. Y. Liang, F. Cao, D. Qi, T. Jia, Z. Sun, S. Zhang, W. Chen, Z. Yin, S. Wang, Z. Han, G. Guo, L. V. Wang, *Adv. Quantum Technol.* **2018**, *1*, 1800034.
[29] A. G. H. Podoleanu, in *Lasers for Medical Applications* (Ed: H. Jelínková), Woodhead Publishing, Sawston, Cambridge **2013**.
[30] M. C. Nadeau, G. Duchateau, M. Dumergue, N. Fedorov, D. Descamps, S. Petit, G. Geoffroy, P. Martin, *J. Opt. Soc. Am. B* **2018**, *35*, 1119.
[31] J. Y. Liang, S. Y. Wu, R. N. Kohn, M. F. Becker, D. J. Heinzen, *Opt. Eng.* **2012**, *51*, 108201.
[32] J. Y. Liang, R. N. Kohn, M. F. Becker, D. J. Heinzen, *J. Micro-Nanolithogr., MEMS, MOEMS* **2012**, *11*, 023002.
[33] P. Daponte, L. D. Vito, G. Mazzilli, F. Picariello, S. Rapuano, M. Riccio, in *2015 IEEE Metrology for Aerospace (MetroAeroSpace)*, IEEE, Benevento, Italy **2015**, p. 306.
[34] L. I. Rudin, S. Osher, E. Fatemi, *Phys. D* **1992**, *60*, 259.
[35] N. Antipa, G. Kuo, R. Heckel, B. Mildenhall, E. Bostan, R. Ng, L. Waller, *Optica* **2018**, *5*, 1.
[36] S. H. Chan, X. Wang, O. A. Elgendy, *IEEE Trans. Comput. Imaging* **2016**, *3*, 84.
[37] S. V. Venkatakrishnan, C. A. Bouman, B. Wohlberg, in *2013 IEEE Global Conf. Signal and Information Processing*, IEEE, Austin, TX, USA **2013**, p. 945.
[38] K. Dabov, A. Foi, V. Katkovnik, K. Egiazarian, presented at SPARS'09 - Signal Processing with Adaptive Sparse Structured Representations, Saint Malo, France, April **2009**.
[39] S. Boyd, N. Parikh, E. Chu, B. Peleato, J. Eckstein, *Found. Trends Mach. Learn.* **2010**, *3*, 1.
[40] U. S. Kamilov, H. Mansour, B. Wohlberg, *IEEE Signal Process. Lett.* **2017**, *24*, 1872.
[41] S. Sreehari, S. V. Venkatakrishnan, B. Wohlberg, G. T. Buzzard, L. F. Drummy, J. P. Simmons, C. A. Bouman, *IEEE Trans. Comput. Imaging* **2016**, *2*, 408.
[42] Y. Sun, S. Xu, Y. Li, L. Tian, B. Wohlberg, U. S. Kamilov, in *ICASSP 2019 - 2019 IEEE Int. Conf. Acoustics, Speech and Signal Processing (ICASSP)*, IEEE, Brighton, United Kingdom **2019**, p. 7665.
[43] S. H. Chan, *IEEE Trans. Comput. Imaging* **2019**, *5*, 274.
[44] H. Xie, I. Ben-Zvi, T. Rao, T. Xin, E. Wang, *Phys. Rev. Accel. Beams* **2016**, *19*, 103401.
[45] O. Siegmund, J. Vallerga, J. McPhate, J. Malloy, A. Tremsin, A. Martin, M. Ulmer, B. Wessels, *Nucl. Instrum. Methods Phys. Res., Sect. A* **2006**, *567*, 89.
[46] J. Liu, Y. Sun, X. Xu, U. S. Kamilov, in *ICASSP 2019 - 2019 IEEE Int. Conf. Acoustics, Speech and Signal Processing (ICASSP)*, IEEE, Brighton, United Kingdom **2019**, p. 7715.
[47] Z. Wu, Y. Sun, A. Matlock, J. Liu, L. Tian, U. S. Kamilov, *IEEE J. Sel. Topics Signal Process.*, unpublished. https://doi.org/10.1109/jstsp.2020.2999820
[48] E. Hontzopoulos, D. Charalambidis, C. Fotakis, G. Farkas, Z. G. Horváth, C. Tóth, *Opt. Commun.* **1988**, *67*, 124.
[49] D. Kozawa, Y. Miyauchi, S. Mouri, K. Matsuda, *J. Phys. Chem.* **2013**, *4*, 2035.

